Chemical Science

ROYAL SOCIETY OF CHEMISTRY

EDGE ARTICLE

View Article Online
View Journal

Cite this: DOI: 10.1039/d5sc07813j

All publication charges for this article have been paid for by the Royal Society of Chemistry

A dicationic ionic liquid strategy to enhance the thermal stability of manganese bromide scintillators

Guo-Yang Chen,[abd] Hao-Wei Lin,[abc] Abdusalam Ablez,[abd] Xin-Pin Guo,[abd] Yu-Wei Ren,[abd] Jia-Hua Luo,[abd] Qing-Hua Zou,[e] Ke-Zhao Du, *[f] Ze-Ping Wang *[a] and Xiao-Ying Huang *[abc]

Conventional organic–inorganic hybrid manganese halides (Mn-OIMHs) as scintillators face challenges in thermal stability. This work proposes a strategy of introducing dicationic ionic liquids (DILs) to construct dicationic Mn-OIMHs with improved thermal stability. Comparative studies for the structures and X-ray scintillation properties are done for a series of Mn-OIMHs, that is, dicationic $AMnBr_4$ (A = $PP214^{2+}$ (1,4-bis(*N*-methylpiperidinyl)-butane) for **1**, $P214^{2+}$ (1,4-bis(*N*-methylpyrrolidinium)-butane) for **3**, and $PP215^{2+}$ (1,5-bis(*N*-methylpiperidinyl)-pentane) for **5**) and monocationic A_2MnBr_4 (A = $PP14^{+}$ (*N*-methyl-*N*-butylpiperidinium) for **2**, $P14^{+}$ (*N*-methyl-*N*-butylpyrrolidinium) for **4**, and $PP15^{+}$ (*N*-methyl-*N*-pentylpiperidine) for **6**). By leveraging the unique "dual charge centers" to enhance the electrostatic interactions and hydrogen bonding forces, the increased structural rigidity not only improves the photoluminescence quantum yield (PLQY) of materials, but also results in significantly enhanced thermal stability, enabling **1** to maintain 86% of its luminescence intensity at 450 K (*vs.* 300 K). Furthermore, compared to **2**/**4**/**6**, the light yield (LY) of **1**/**3**/**5** is increased by several fold. Finally, a flexible scintillation film fabricated by embedding **1** in polydimethylsiloxane (PDMS) achieves a spatial resolution of 14.1 lp mm^{-1}, surpassing that of commercial CsI:Tl detectors (~10 lp mm^{-1}). This work provides an effective design strategy for the preparation of Mn-based X-ray scintillators with high thermal stability and excellent photophysical properties.

Received 9th October 2025
Accepted 12th January 2026

DOI: 10.1039/d5sc07813j

rsc.li/chemical-science

Introduction

High-temperature scintillators are indispensable for radiation detection in extreme environments such as petroleum exploration, space nuclear missions, and reactor monitoring.[1,2] As core detector components, they require high light yield (LY), exceptional thermal stability, and mechanical robustness. Current high-temperature scintillators, including traditional scintillators (NaI:Tl,[3] CsI:Tl,[4] and $LaBr_3$:Ce[5]) and commercial scintillators (YAg:Ce,[6] LuAg:Ce,[7] and BGO[8]) rely on energy-intensive solid-state synthesis (>1000 °C). This complex manufacturing process results in prohibitively high costs, severely limiting scalability.[9] While organic scintillators (anthracene, polystyrene, and triphenylmethane)[10–12] offer cost advantages through low-temperature synthesis, their inherent limitations intensified molecular thermal motion and insufficient stability at elevated temperatures, which preclude reliable high-temperature operation. Addressing this challenge demands new scintillator materials synergizing high performance, thermal stability, and economically viable processing.[13–15]

Organic–inorganic metal halides (OIMHs) have broad application prospects in solid state lighting,[16,17] optical anti-counterfeiting,[18,19] radiation detection,[13] X-ray scintillation,[20,21] and other fields, due to their excellent luminescent properties. In recent years, traditional monocationic ionic liquids (MILs), which are composed of a single organic cation (such as pyridinium, piperidine, and quaternary ammonium salts) paired with anions (such as Cl^-, $[BF_4]^-$, and $[PF_6]^-$) have emerged as the preferred platform for designing the organic components of OIMHs due to their structurally tunable cation, rich anion library, and excellent dissolution and processing performance.[18,19] Various low-dimensional luminescent OIMHs based on metal ions of tin(II) (Sn^{2+}),[22] copper(I) (Cu^+),[23] antimony(III) (Sb^{3+}),[24] bismuth(III) (Bi^{3+}),[20] zinc(II) (Zn^{2+}),[25] and manganese(II) (Mn^{2+})[26,27] have been developed based on MILs. Among them,

[a]State Key Laboratory of Structural Chemistry, Fujian Institute of Research on the Structure of Matter, The Chinese Academy of Sciences, Fuzhou, Fujian, 350002, China. E-mail: xyhuang@fjirsm.ac.cn; wzping520@msn.cn

[b]Fujian College, University of Chinese Academy of Sciences, Fuzhou, Fujian, 350002, China

[c]University of Chinese Academy of Sciences, Beijing, 100049, China

[d]College of Chemistry Fuzhou University, Fuzhou, Fujian, 350108, China

[e]Jiangxi University of Science and Technology, Ganzhou 341000, China

[f]Fujian Provincial Key Laboratory of Advanced Materials Oriented Chemical Engineering, College of Chemistry and Materials Science, Fujian Normal University, Fuzhou, 350007, China. E-mail: duke@fjnu.edu.cn

manganese-based OIMHs (Mn-OIMHs) have become important candidates for X-ray scintillation applications owing to their high photoluminescence quantum yield (PLQY > 50%) from d–d transitions, low-cost processability, and environmental friendliness.[14] However, traditional Mn-OIMHs synthesized based on MILs (typically with isolated tetrahedral $[MnX_4]^{2-}$ units) exhibit severe thermal quenching at elevated temperatures, where enhanced lattice vibrations dominate non-radiative transition pathways, leading to drastic luminescence intensity reduction and ultimately limiting their high-temperature applications.[28,29] Therefore, developing Mn-OIMHs with minimal energy loss and anti-thermal quenching (ATQ) at high temperatures has become a key area of current research.

Substantial research efforts have been devoted to optimizing the ATQ performance of organic–inorganic hybrid metal halides by enhancing structural rigidity, forming a clear research trajectory.[30–33] Strengthening hydrogen bonding has been identified as an effective strategy, as demonstrated by Ye *et al.* in their study of $C_5H_6NMnCl_3 \cdot H_2O$, where enhanced hydrogen bonding between the pyridine ring and the 1D $Mn(Cl/O)_6$ chains resulted in a more rigid lattice that suppressed molecular vibrations and reduced non-radiative transitions, thereby improving ATQ performance.[34] Subsequently, Li *et al.* successfully enhanced the structural rigidity of 2D Dion-Jacobson phase perovskites by incorporating diammonium cations into $MAPbI_3$, leveraging alternating hydrogen bonds with the inorganic slabs.[35] On the other hand, enhancing electrostatic interactions has also proven to be an effective approach for structural stabilization. For instance, Wang *et al.* introduced diphenyl guanidinium bromide (DPGABr) as a passivator, which significantly improved material stability by strongly anchoring halide anions *via* robust electrostatic interactions with the $[PbX_6]^{4-}$ framework.[36] Zhou *et al.* proposed a local electrostatic interaction strategy by employing a previously unexplored and rationally designed organic cation—tetramethyl dipropylenetriamine ($IDPA^{2+}$). This cation enables strong local electrostatic interactions with the $[PbI_6]^{4-}$ octahedra, thereby inducing lattice compression in the perovskite structure and subsequently enhancing its structural stability.[37] Based on this mechanism, we propose a "dual charge centers" design concept, that is, introducing dicationic ionic liquids (DILs) with two positively charged centers to prepare dicationic Mn-OIMHs with enhanced structural rigidity and thereby significant ATQ performance. This design simultaneously achieves two objectives: enhancing overall electrostatic interactions through high charge density[38] and maintaining a suitable positive electrostatic potential on the molecular surface to promote the formation of a directed hydrogen-bonding network.[39,40] This synergistic effect is expected to provide an ideal platform for fabricating dicationic Mn-based OIMHs with rigid structures and excellent ATQ performance. Although dicationic hybrid metal halides were previously reported[41,42] and have shown outstanding luminescence and scintillation performance, their thermal stability remains largely neglected. A systematic comparison of the structure–property relationships between dicationic structures and their monoatomic counterparts is even scarcer.

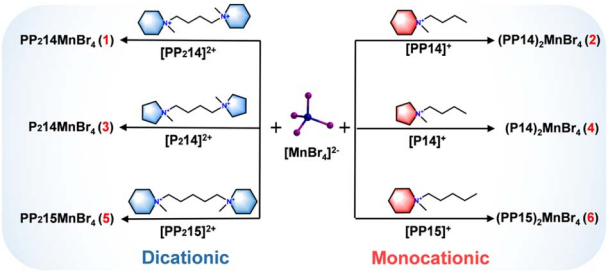

Scheme 1 Assembly pathways for compounds **1**–**6**.

In this work, we successfully synthesized a series of dicationic Mn-OIMHs *via* solvothermal and ether diffusion methods, namely $AMnBr_4$ (A = $PP214^{2+}$, 1,4-bis(*N*-methylpiperidinyl)-butane for **1**; $P214^{2+}$, 1,4-bis(*N*-methylpyrrolidinyl)-butane for **3**; $PP215^{2+}$, 1,5-bis(*N*-methylpiperidinyl)-pentane for **5**). For comparison, a series of corresponding monocationic Mn-OIMHs were synthesized, namely A_2MnBr_4 (A = $PP14^+$, *N*-methyl-*N*-butylpiperidinium for **2**;[43] $P14^+$, *N*-methyl-*N*-butylpyrrolidinium for **4**;[43] $PP15^+$, *N*-methyl-*N*-pentylpiperidine for **6**) (Scheme 1). Electrostatic potential (ESP) analysis indicates that the dicationic structure **1** exhibits stronger electrostatic interactions and a more abundant hydrogen bond network than monocationic structure **2**, thereby conferring it with a more rigid structure. This feature of dicationic structures effectively suppresses non-radiative transitions, stabilizes the luminescent center and significantly enhances their PLQY. Consequently, the enhanced structural rigidity enables **1** to exhibit outstanding ATQ behavior, with the luminescence intensity at 450 K retaining 86% of its value at 300 K, while that of **2** only maintains 5%. Furthermore, dicationic Mn-OIMHs **1**/**3**/**5** exhibited a significantly enhanced light yield (LY) of 42 500, 13 420, and 21 132 ph MeV^{-1}, respectively, under X-ray irradiation. These values represent 3.6-, 1.6-, and 1.9-fold increases compared to that of their monocationic counterparts (compounds **2**/**4**/**6**). Notably, the flexible scintillation film fabricated by incorporating **1** with polydimethylsiloxane (PDMS) achieves a spatial resolution of 14.1 lp mm^{-1}, significantly surpassing that of commercial CsI:Tl detectors (~10 lp mm^{-1}). These results demonstrate that the incorporation of DILs indeed effectively enhances the structural rigidity and performance of Mn-OIMHs, validating the design rationale derived from our prior theoretical analysis.

Results and discussion

Structure and characterization

All MILs and DILs used for the synthesis of title compounds were obtained by simple organic synthesis, as detailed in Scheme S1. Single crystals of compounds **1**–**6** were successfully obtained through simple solvothermal or ether diffusion methods. As representative examples, compounds **1** and **2** form block-shaped crystals under ambient light conditions that exhibit bright green luminescence under UV irradiation (Fig. S1). Single-crystal X-ray diffraction analysis shows that compound **1** crystallizes in the monoclinic space group $P2_1/c$,

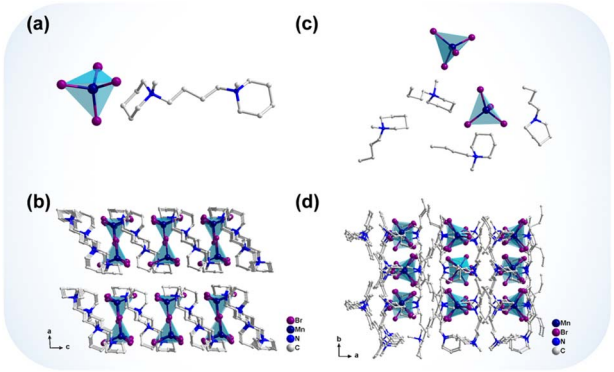

Fig. 1 (a) The asymmetric unit of compound **1**. (b) The packing diagram of **1** viewed along the *b*-axis. (c) The asymmetric unit of compound **2**. (d) The packing diagram of **2** viewed along the *c*-axis. Hydrogen atoms are omitted for clarity.

with $[MnBr_4]^{2-}$ anions intercalated between $[PP214]^{2+}$ cations (Fig. 1a and b). By contrast, compound **2** adopts the *C*2/*c* space group and contains discrete $[MnBr_4]^{2-}$ anions separated by $[PP14]^{+}$ cations (Fig. 1c and d).[43] Detailed structural analysis (Tables S1 and S4–S6) reveals that the $[MnBr_4]^{2-}$ units in compound **1** exhibit nearly ideal tetrahedral geometry, with uniform Mn–Br bond lengths ranging from 2.502 to 2.510 Å and Br–Mn–Br angles between 106.99° and 114.75°. On the other hand, the $[MnBr_4]^{2-}$ tetrahedra in compound **2** show significant distortion, reflected by Mn–Br bond lengths varying from 2.401 to 2.583 Å and Br–Mn–Br angles ranging from 100.9° to 123.1°. Complete structural data for compounds **3–6** are provided in Fig. S2 and S3.

We then calculated the aberrations of the individual $[MnBr_4]^{2-}$ tetrahedra in **1–6** using eqn (1) for bond angle aberrations (σ^2) and eqn (2) for bond length aberrations (Δd):[44,45]

$$\sigma^2 = \frac{1}{5}\sum_{n=1}^{6}(\theta_n - 109.47^\circ)^2 \quad (1)$$

$$\Delta d = \frac{1}{4}\sum_{n=1}^{4}\left[\frac{d_n - d}{d}\right]^2 \quad (2)$$

where θ_n is the Br–Mn–Br bond angle, d_n is the Mn–Br bond length, and d is the average Mn–Br bond length. Taking **1** and **2** as examples, calculations show that the $[MnBr_4]^{2-}$ of **1** exhibits smaller distortion. Its bond length distortion is 1.39×10^{-6}, and its bond angle distortion is 8.13. By contrast, the $[MnBr_4]^{2-}$ in compound **2** exhibits greater distortion, with a bond length distortion of 4.16×10^{-4} and a bond angle distortion of 40.03, consistent with its previously described structural characteristics (Fig. 2a). As indicated in Fig. 2b, dicationic structures **1**/**3**/**5** exhibit a higher crystal density (ρ) than monocationic structures **2**/**4**/**6**. This suggests more efficient molecular packing, likely due to enhanced intermolecular interactions, as evidenced by the consistently higher Crystal Packing Index (CPI) and Kitaigorodskii's Packing Index (KPI)[46,47] values for compounds **1**/**3**/**5** than for compounds **2**/**4**/**6** (see Table S7 for detailed calculations). Additionally, the dicationic structures with smaller bond angle distortions (σ^2) and a denser environment exhibit superior photophysical properties, as primarily manifested in improved PLQY and LY (Fig. 2c–e).

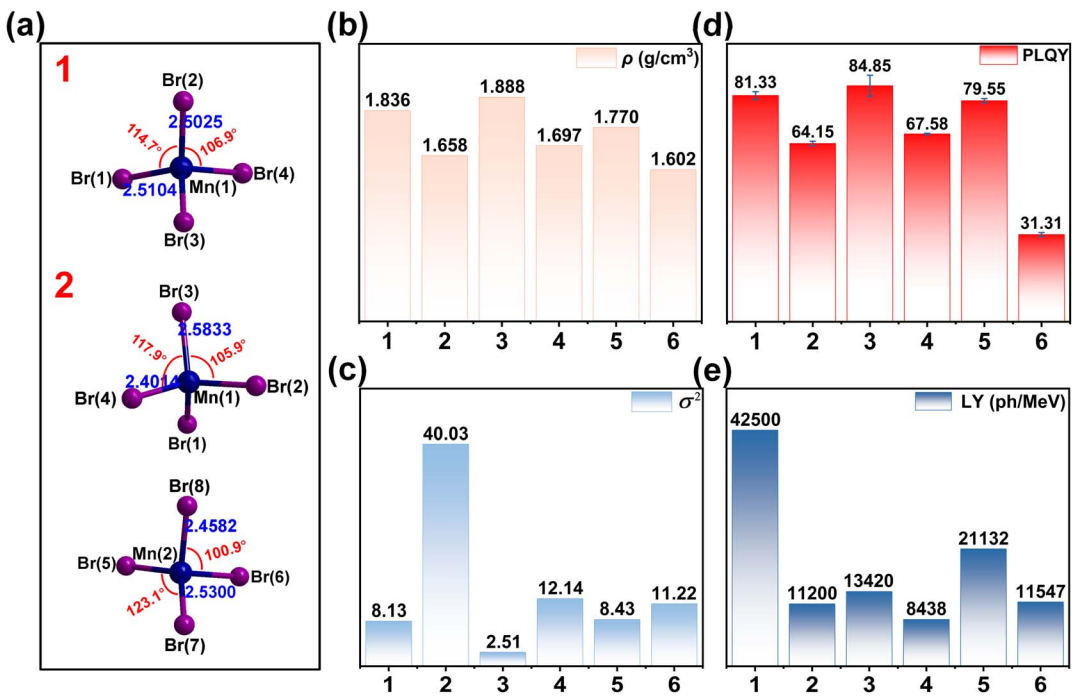

Fig. 2 (a) Diagrams showing the bond lengths (Å) and bond angles of the $[MnBr_4]^{2-}$ tetrahedra in compounds **1** and **2**. Comparison of (b) the crystal density (ρ) and (c) bond angle distortion (σ^2) for compounds **1–6**. (d) Comparison of the PLQY for compounds **1–6**. Error bars indicate the standard deviation of three independent measurements. (e) Comparison of the LY for compounds **1–6**.

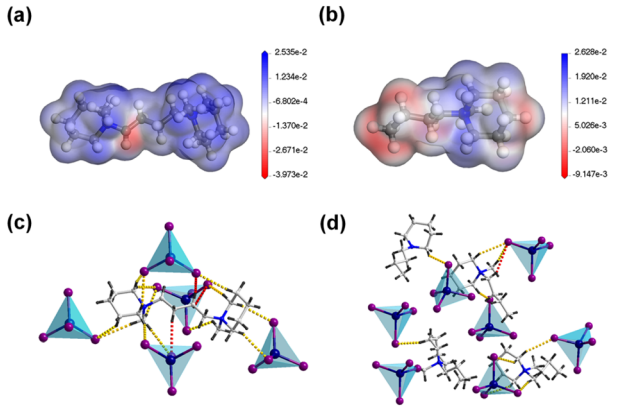

Fig. 3 Visualization of the surface electrostatic potential of cations $PP214^{2+}$ in **1** (a) and $PP14^{+}$ in **2** (b). Schematic diagrams of hydrogen bonding interactions around cations $PP214^{2+}$ in **1** (c) and $PP14^{+}$ in **2** (d). The yellow and red dashed lines represent hydrogen bonds acting on the piperidine ring and alkyl chain, respectively.

We have conducted an in-depth investigation into the mechanisms by which "dual charge centers" influence the structural rigidity. The introduction of dual charge centers (N^{+}) in a dicationic structure significantly reshapes the molecular electrostatic potential (ESP) distribution. For systems driven by electrostatic interactions, ESP analysis provides critical mechanistic insights. In cationic systems, regions with high positive ESP (typically displayed as blue isosurfaces) exhibit enhanced electron affinity and dominate anion binding.[38] Fig. 3a and b show that the positive ESP regions (blue) of the $PP214^{2+}$ cation are significantly expanded compared to those of the $PP14^{+}$ cation, indicating stronger electrostatic attraction to the $[MnBr_4]^{2-}$ anion. Additionally, the ESP analysis results can help us infer hydrogen bonding sites.[38,48] It can be observed that the alkyl chain surface of the $PP14^{+}$ cation exhibits a distinct negative ESP (red), indicating a high electron density in this region that repels the surrounding $[MnBr_4]^{2-}$ and inhibits hydrogen bond formation. The piperidine ring region exhibits weak positive ESP (blue–white), with a more dispersed electron distribution, making it easier to form hydrogen bonds with the surrounding $[MnBr_4]^{2-}$. Therefore, in the monocationic structures, hydrogen bonds are mainly formed between the piperidine ring and the $[MnBr_4]^{2-}$ unit. By contrast, the $PP214^{2+}$ cation not only exhibits a significant positive ESP (blue) in both piperidine ring regions but also maintains a weak positive ESP (blue–white) across the entire alkyl chain surface under the synergistic neutralization of the dual high-charge centers (N^{+}). This allows both the piperidine rings and alkyl chains to potentially form hydrogen bonds with the surrounding $[MnBr_4]^{2-}$. When examining the hydrogen bonds on the organic cation portions of **1** and **2** (Fig. 3c and d), it is evident that the hydrogen bonds of the $PP14^{+}$ cation in **2** primarily act on the piperidine rings, while the hydrogen bonds of the $PP214^{2+}$ cation in **1** not only act on the two piperidine rings but also exhibit a significantly higher number of hydrogen bonds on the alkyl chain compared to the $PP14^{+}$ cation, which effectively validates the previous statement. For compounds **3–6**, the hydrogen bonding sites on the cation surface confirm the universality of this strategy in enhancing structural rigidity (Fig. S4a–d).

Hirshfeld surface and two-dimensional fingerprint analyses further elucidate the weak interactions between the organic cations and $[MnBr_4]^{2-}$ tetrahedra.[49,50] Regions of long-range weak interactions are depicted in blue, while short–range interactions are highlighted in red. As shown in Table S6, the bond lengths of all C–H···Br hydrogen bonds are approximately 3 Å. To quantitatively analyze these interactions, we analyzed the two-dimensional fingerprint spectra, focusing on the cationic region ($(d_e, d_i) = (1.2\ Å, 1.8\ Å)$) and the anionic region ($(d_i, d_e) = (1.8\ Å, 1.2\ Å)$). Significant differences were observed in these regions: the density of red data points (representing C–H···Br contacts) is notably higher in **1** than in **2**, clearly indicating a higher abundance of C–H···Br hydrogen bonds in the crystal structure of **1** (Fig. S5 and S6). This result is consistent with the rigid structural environment of **1**. The Hirshfeld surfaces and two-dimensional fingerprint analysis diagrams for compounds **3–6** are shown in Fig. S7–S10, and the results are consistent with those for **1** and **2**.

The above results qualitatively demonstrate that the dual charge centers play a crucial role in the dicationic structure: increasing the charge density through the dual positive charge enhances the electrostatic interactions with the inorganic anion framework. Additionally, the extra hydrogen bonding sites lead to a more abundant hydrogen bonding network, thus enhancing structural rigidity. The combined effect of these two factors results in a more compact crystal structure, as evidenced by the difference in crystal density (Fig. 2b).

The PXRD patterns of the powder crystals are in agreement with the theoretical simulations, indicating the high purity of the grown single-crystal phases (Fig. S11). According to the thermogravimetric analysis (TGA) curves, **1** starts to decompose at 335 °C, while **2** starts to decompose at 290 °C. The thermal decomposition temperature of **1** is significantly higher than that of **2**, which is closely related to the more rigid structure of dicationic OIMHs (Fig. S12), providing a new strategy for the preparation of highly thermally stable Mn-OIMHs.

Photoluminescence (PL) and scintillation properties

To investigate the PL properties of these halides, we conducted comprehensive steady-state and time-resolved PL measurements (Fig. 4a and S13). Both **1** and **2** exhibit similar excitation and emission profiles, with maximum emission peaks centering at 520 nm under 363 nm excitation, characteristic of the Mn^{2+} d–d transition ($^4T_1 \rightarrow {}^6A_1$). The emission spectra show FWHM values of 49 nm for **1** and 63 nm for **2**, with corresponding CIE coordinates of (0.214, 0.692) and (0.274, 0.656), respectively (Fig. S14). Time-resolved measurements reveal comparable decay times of 341 μs for **1** and 351 μs for **2**, respectively, Fig. 4b. The emission wavelength remains constant at 520 nm across excitation wavelengths from 290–410 nm, confirming Mn^{2+} as the sole emission center (Fig. S15a and b). The PLQYs of all compounds were determined from three independent measurements, with the average value reported as the final

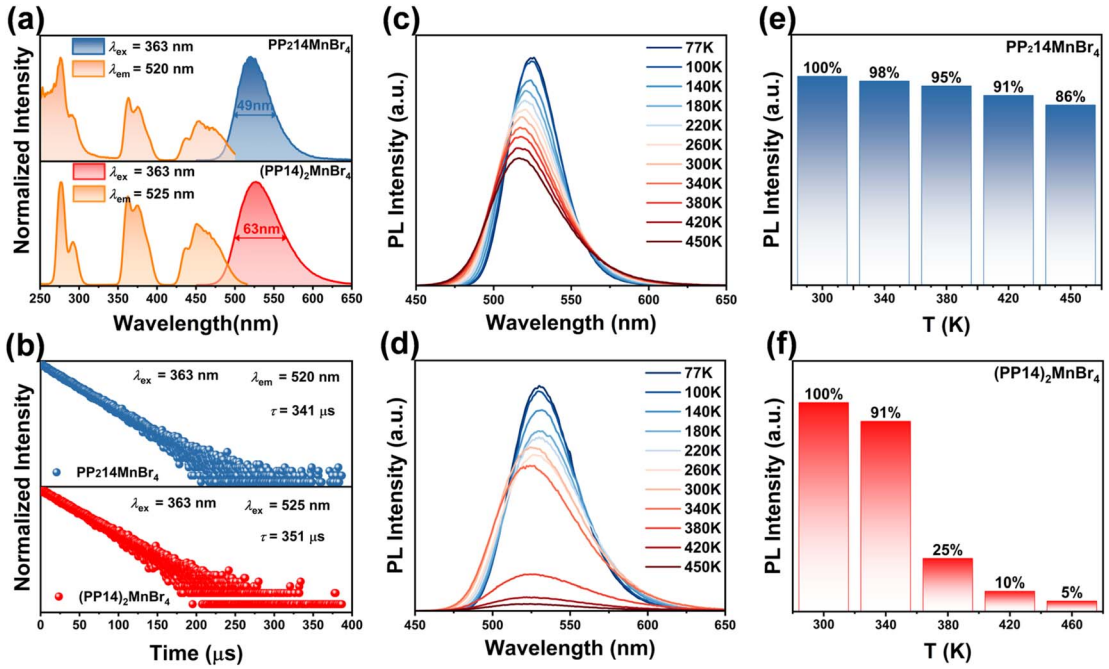

Fig. 4 (a) Excitation and emission spectra of compounds **1** and **2**. (b) Fitted lifetimes of compounds **1** and **2**. Variable temperature emission spectra of compounds **1** (c) and **2** (d) at 77–450 K. Comparison of PL intensity at different temperatures for compounds **1** (e) and **2** (f) relative to 300 K.

result. The measured PLQY values varied considerably across the series, reaching 81.33% for **1** and 67.15% for **2** (Fig. S16). While both possess suitable Mn–Mn distances (9.367 Å for **1** and 9.849 Å for **2**) (Fig. S17), which minimize energy transfer between Mn centers and thus exert limited influence on PLQY,[14,51] the key distinction lies in the differing degrees of structural distortion. The $[MnBr_4]^{2-}$ tetrahedron in compound **2** exhibits markedly enhanced bond angle distortion, which is the primary factor accounting for the disparity in its PLQY. Lattice distortion perturbs the energy levels of Mn^{2+} ions, introducing disordered states that substantially influence the luminescence transition process.[52] This enhances non-radiative recombination pathways and reduces the effective emission of photons. By contrast, the lower lattice distortion of the $[MnBr_4]^{2-}$ tetrahedron in compound **1** effectively suppresses non-radiative transitions, thereby enhancing luminescence intensity and PLQY. Furthermore, compared to the flexible structure of **2**, the enhanced structural rigidity of **1** arises from strong electrostatic interactions and abundant hydrogen bonding sites on its alkyl chains. This rigidity stabilizes luminescent centers, suppresses non-radiative transitions *via* a molecular confinement effect, and ultimately elevates the PLQY of **1**. Additionally, based on PLQY and lifetime, the radiation decay rate (k_r) and non-radiative decay rate (k_{nr})[53,54] calculated using eqn (S1) and (S2) are summarized in Table S8. The PLQY is highly dependent on the competition between k_r and k_{nr}. The k_r for **1** is approximately twice that of **2**, while the k_{nr} is only one-quarter of that for **2**, resulting in the higher PLQY of **1**. Overall, we conclude that the enhancement of PLQY is due to a combination of the smaller bond angle distortion of the dicationic structure and the rigid environment of the structure.

The temperature-dependent PL spectra of **1** and **2** were systematically studied in the temperature range of 77–450 K (Fig. 4c–f). For compound **1**, strong emission is maintained across the entire temperature range, with only a slight decrease in intensity and a gradual blue shift. At 450 K, the PL intensity remains as high as 86% of that at 300 K. This high thermal stability can be attributed to the stronger cation–anion interactions in **1**, which suppress ionic motion through enhanced binding. By contrast, compound **2** exhibits a gradual decrease in PL intensity with increasing temperature, which is ascribed to enhanced lattice vibrations that promote lattice relaxation of the $[MnBr_4]^{2-}$ luminescent centers, thereby suppressing exciton recombination.[55] Between 77 and 300 K, the emission peak of **1** shifts gradually to longer wavelengths due to the magnetic coupling of Mn^{2+} clusters.[56] The PL intensity of compound **2** decreases more sharply between 340 and 380 K than that of compound **1**. To understand this TQ behavior, we performed variable-temperature PXRD measurements (Fig. S18 and S19). For compound **2**, a marked broadening in peak width (FWHM) is observed within this temperature range, implying enhanced local structural disorder induced by intensified thermal motions of the organic cations. Such disorder dynamically disrupts the coordination environment of the Mn^{2+} centers, promoting non-radiative decay and leading to the observed rapid decline in emission intensity.[57] Furthermore, under the same experimental conditions, four complete heating–cooling cycles of photoluminescence spectroscopy were performed for compounds **1** and **2** between 300 K (cooling point) and elevated temperatures of 350, 400, and 450 K. The collected data are presented in Fig. S20. Throughout multiple cycles, the luminescence intensity of compound **1** remains highly consistent

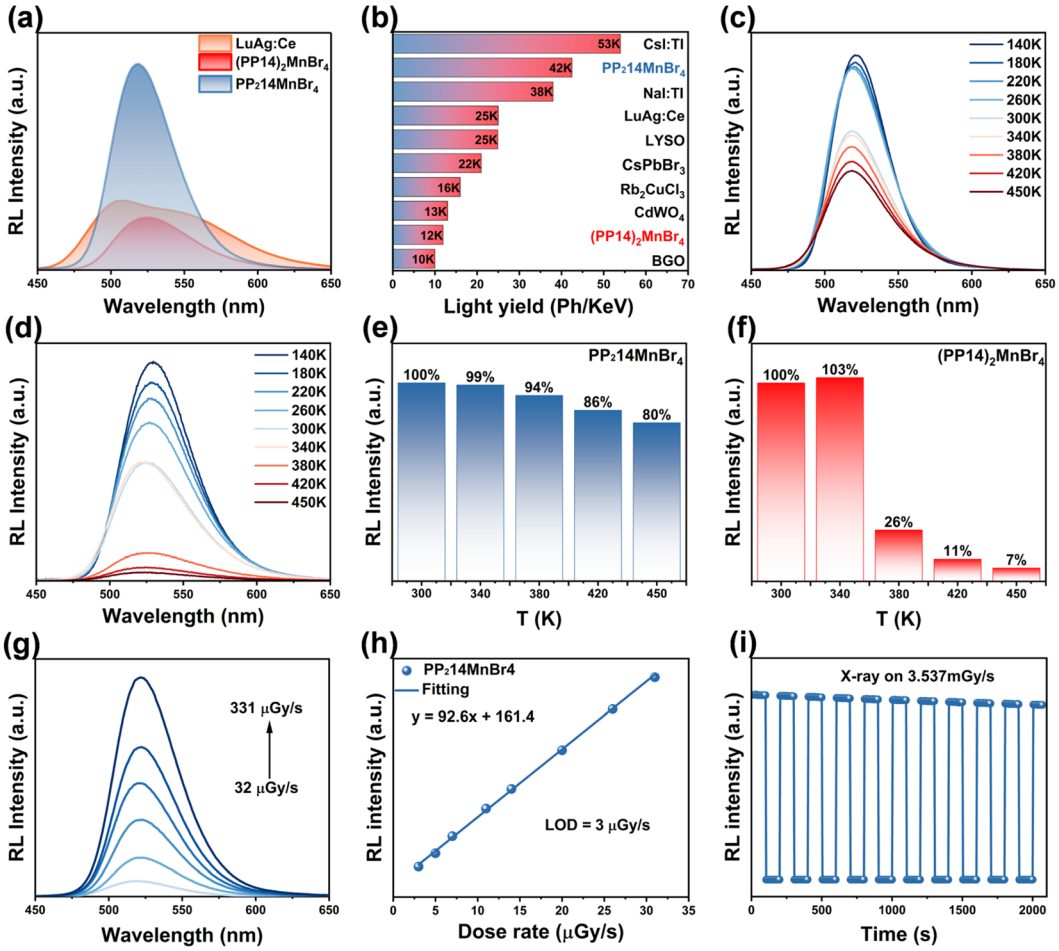

Fig. 5 (a) RL emission spectra of compounds **1**, **2** and LuAg:Ce under X-ray irradiation. (b) Comparison of the LY of compounds **1** and **2** with those of common commercially available inorganic scintillators. Variable temperature RL emission spectra of compounds **1** (c) and 2 (d) at 140–450 K. Comparison of RL intensity at different temperatures for compounds **1** (e) and **2** (f) relative to 300 K. RL intensities of compound **1** under X-ray irradiation at different doses (32–331 μGy s^{-1}) (g) and the LOD at a SNR of 3 (h). (i) X-ray irradiation stability of compound **1** after 11 cycles of X-ray irradiation at a dose of 3.537 mGy s^{-1}. In each cycle, X-ray irradiation was turned on for 20 s and then off for 20 s.

and fully reversible, with no signs of irreversible degradation, which confirms its excellent thermal stability. We compared several recently reported hybrid halides containing the $[MnBr_4]^{2-}$ unit and calculated the ratio of the PL intensity at the maximum measured temperature to that at room temperature (300 K) using temperature-dependent fluorescence data (Fig. S21). Notably, compound **1** demonstrates ATQ performance, surpassing that of most reported $[MnBr_4]^{2-}$-based hybrids. This excellent behavior originates from the structural design of the $PP214^{2+}$ cation: its high charge density strengthens electrostatic interaction with the $[MnBr_4]^{2-}$ framework, while the dual N^+ centers enable the alkyl chains to form additional hydrogen bonding sites, thereby restraining vibrational disorder of the cation. These combined effects enhance the structural rigidity, stabilize the $[MnBr_4]^{2-}$ emitter, and effectively suppress thermal non-radiative decay.

To confirm that the outstanding ATQ performance of $PP214MnBr_4$ originates from its rigid structure, we performed systematic variable-temperature X-ray diffraction analyses. Variable-temperature XRD (Fig. S18) shows that even when heated to 450 K, the diffraction peaks undergo no significant changes, collectively demonstrating excellent structural stability at the macroscopic level. Furthermore, single-crystal data collected at 300 K and 450 K (Table S9) confirm that the crystal structure remains consistent throughout the heating process, ruling out any influence of phase transitions on the ATQ behavior. More importantly, geometric analysis of the $[MnBr_4]^{2-}$ tetrahedron between 77 K and 450 K (Tables S10 and S11) reveals minimal changes in bond lengths, bond angles, and structural distortion, providing atomic-scale evidence of its intrinsic structural rigidity. In summary, both the variable-temperature XRD and SCXRD results consistently indicate that the thermal stability and ATQ behavior of $PP214MnBr_4$ over a broad temperature range can be attributed to its remarkable structural rigidity spanning from the microscopic chemical bonds to the macroscopic crystal lattice.

In addition, the potential barrier between the radiative and non-radiative centers, defined as the thermal activation energy (E_a), serves as a measure of the ability to overcome the thermal quenching effect. A larger E_a value indicates greater exciton

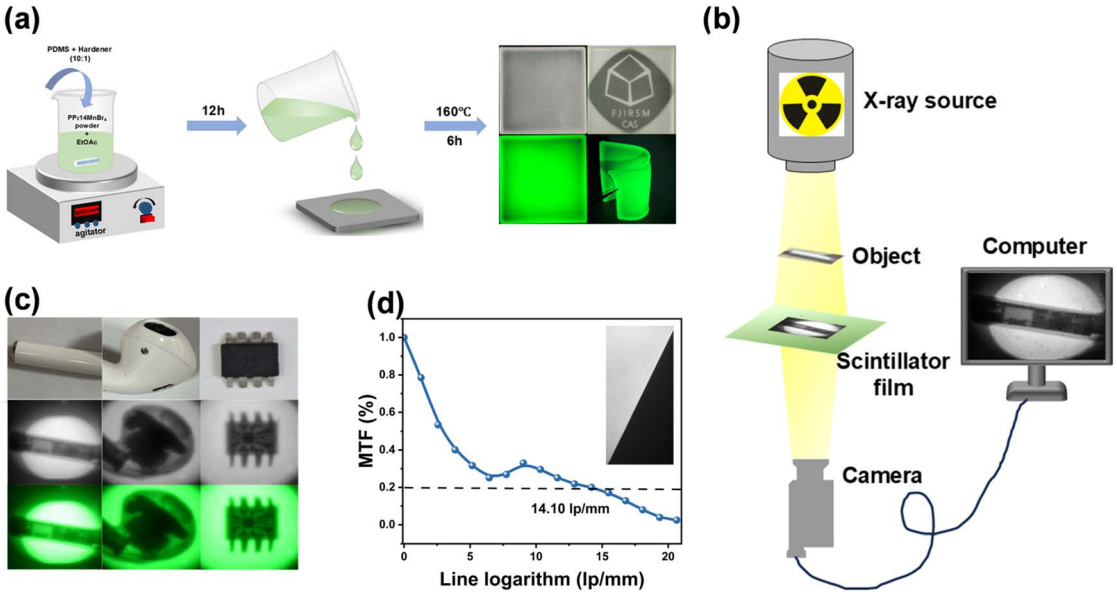

Fig. 6 (a) Process for the preparation of scintillator films using compound **1** and a 5 cm × 5 cm presentation view under ambient light *vs.* UV light. (b) Schematic diagram of a homemade X-ray imaging device. (c) X-ray imaging photographs of the headset and the chip. (d) MTF of **1** of the scintillator film beveled edge image showing a spatial resolution of 14.1 lp mm^{-1}.

stability, higher radiative transition rates, and stronger resistance to thermal quenching.[58,59] The exciton dynamics of **1** and **2** were investigated using eqn (3):[60]

$$I_0/I_{(T)} = 1 + A\exp^{-E_a/K_bT} \quad (3)$$

where I_0 and $I_{(T)}$ represent the intensity at 77 K and the measured PL intensity at different temperatures, respectively. During the fitting process, the integrated area of the PL spectrum is used as a substitute, and K_b is the Boltzmann constant. The fitted E_a values of 214 meV (**1**) and 186 meV (**2**) (Fig. S22a and b) demonstrate that the reasonable structural design creates a higher potential barrier between radiative and non-radiative centers for **1**. This enhanced E_a effectively prevents thermal dissociation, accounting for thermal-resistant PL quenching of **1**. Under the promotion of the dual *N*-methylpiperidine rings, it reduces the disordered vibrations of the alkyl chains and effectively prevents exciton dissociation, resulting in higher RL intensities.[61]

The X-ray absorption and radioluminescence properties of compounds **1–6** were further investigated. The absorption rates of high-energy X-ray photons (1 keV to 100 keV) for **1–6** are of the same order of magnitude as those of the commercial scintillator LuAg:Ce (Fig. S23a–c). The X-ray attenuation efficiency of compounds with different thicknesses was also measured, showing an 80% X-ray attenuation efficiency at a thickness of 0.4 mm (Fig. S23d–f). Under X-ray excitation (3.537 mGy s^{-1}), the RL spectra of **1–6** closely match their PL profiles, confirming identical emission pathways for both UV and X-ray excitation (Fig. S24a–f). Quantitative analysis of the RL spectra (Fig. 5a and S25a–c) reveals a LY of 42 500 photons ph MeV^{-1} for **1** and 11 968 ph MeV^{-1} for **2**. The scintillation performance of compounds **1** and **2** was benchmarked against that of recently reported Mn-based hybrid metal halide scintillators (Table S12), inorganic scintillators and key commercial references (Fig. 5b). Specifically, the LY of compound **1** is superior to that of commercial benchmarks such as BGO (9000 ph MeV^{-1})[8] and LYSO (24 900 ph MeV^{-1})[62] and emerging halide-based scintillators like Rb_2CuCl_3 (16 600 ph MeV^{-1})[63] and $CsPbBr_3$ quantum dots (21 000 ph MeV^{-1}).[64] The excitation source of X-rays has a high energy, resulting in an increasing temperature during the scintillation test. Therefore, we performed RL measurements of the temperature dependence of **1** and **2**. The samples were placed on a heating device under the X-ray source and the radioluminescence was collected using a fiber optic spectrometer. As shown in Fig. 5c–f, **2** exhibits nearly complete RL luminescence quenching at 450 K, while **1** demonstrates excellent ATQ behavior. RL luminescence intensity only decreases by about 20% at 450 K (*vs.* 300 K). The intensity of the radioluminescence enhances linearly with the increase in the X-ray dose rate (Fig. 5g). Additionally, **1** demonstrates exceptional sensitivity for low-dose detection with a minimum detectable X-ray dose rate of 3.0 μGy s^{-1} at a signal-to-noise ratio (SNR) of 3, which is below the threshold for diagnostic X-ray imaging (5.5 μGy s^{-1}) (Fig. 5h). Remarkably, under prolonged irradiation (30 min at 3.537 mGy s^{-1}), **1** maintains stable RL intensity without significant degradation, highlighting its robust radiation hardness and potential for practical X-ray imaging applications (Fig. 5i).

X-ray imaging

To better study the potential application of **1** in X-ray imaging, we prepared a uniform flexible film with dimensions of 5 × 5 × 0.2 mm using a powder of **1** and polydimethylsiloxane (PDMS). The flexible film exhibits high transparency and emits a bright green light under ultraviolet light (Fig. 6a). We constructed

a simple X-ray imaging system consisting of an X-ray source, an imaging object, a **1**@PDMS scintillator, and a commercial camera connected to a computer display (Fig. 6b). As shown in Fig. 6c, we used a chip and headphones as detection targets to determine the X-ray imaging detection capability, and the internal structures of all samples could be clearly observed. To evaluate the imaging quality, we calculated the modulated transfer function (MTF) of the X-ray image of the inclined edge. The calculated spatial resolution was 14.10 lp mm^{-1} (MTF = 0.2) (Fig. 6d), outperforming the spatial resolution of CsI:Tl (10 lp mm^{-1}),[65] $CsPbBr_3$ (9.8 lp mm^{-1}),[66] and $MAPbBr_3$ (3.1 lp mm^{-1}),[67] which implies a better potential application in X-ray imaging and detection.

Conclusions

In summary, we propose a strategy of incorporating cations of custom-designed dicationic ionic liquids into Mn-OIMHs to enhance their structural rigidity, thereby significantly improving the ATQ performance. ESP analysis reveals the mechanism behind the enhanced structural rigidity: on one hand, the high charge density generated by the "dual charge centers" significantly strengthens the electrostatic interactions between the organic cations and the anionic framework; on the other hand, the high charge nuclei (N^+) neutralize the electron-rich alkyl chains, promoting hydrogen bond formation with Br^-. The synergistic effect of enhanced electrostatic interactions and hydrogen bonding endows the dicationic Mn-OIMHs with a rigid structure and thus not only enhances PLQY but also enables **1** to maintain 86% of its luminescence intensity at 450 K (*vs.* 300 K), achieving excellent ATQ behavior. Moreover, the strategy enhances the LY of Mn-OIMHs, with compounds **1**/**3**/**5** achieving a LY of 42 500, 13 420, and 21 132 ph/MeV, respectively, significantly higher than that of their monocationic counterparts (**2**/**4**/**6**). Additionally, the PDMS flexible film based on 1 exhibits high spatial resolution (14.1 lp mm^{-1}), confirming its high scintillator performance. This work not only establishes a new design paradigm for high-PLQY Mn-OIMHs but also lays a crucial material foundation for developing highly thermally stable and cost-effective X-ray imaging devices.

Author contributions

G. Y. C., K. Z. D., Z. P. W. and X. Y. H. conceived the project. G. Y. C. designed and performed most of the experiments. H. W. L. organized the manuscript. A. A., X. P. G., and Y. W. R. provided helpful discussion of the mechanism. J. H. L, and Q. H. Z. provided assistance in sample preparation and experimental characterization. G. Y. C. prepared the manuscript. G. Y. C., K. Z. D., Z. P. W. and X. Y. H. revised the manuscript. All authors discussed the results and commented on the manuscript. K. Z. D., Z. P. W. and X. Y. H. supervised the project.

Conflicts of interest

There are no conflicts to declare.

Data availability

CCDC 2475506 (**3**), 2475507 (**6**), 2475508 (**5**), 2475509 (**1**), 2514806 (**1–300 K**) and 2514807 (**1–450 K**) contain the supplementary crystallographic data for this paper.[68a-f]

The authors have cited additional references within the supplementary information (SI). Supplementary information: the experimental section, characterization techniques, equations, additional crystal structure descriptions, summary data tables, and supplementary figures. See DOI: https://doi.org/10.1039/d5sc07813j.

Acknowledgements

The authors gratefully acknowledge the financial support provided by the National Natural Science Foundation of China (No. 92261115, 22205236, and 22373014).

Notes and references

1 Y. Wang, M. Li, Z. Chai, Y. Wang and S. Wang, *Angew. Chem., Int. Ed.*, 2023, **62**, e202304638.
2 Q. Zhou, W. Li, J. Xiao, A. Li and X. Han, *Adv. Funct. Mater.*, 2024, **34**, 2402902.
3 Q. Chen, J. Wu, X. Ou, B. Huang, J. Almutlaq, A. A. Zhumekenov, X. Guan, S. Han, L. Liang, Z. Yi, J. Li, X. Xie, Y. Wang, Y. Li, D. Fan, D. B. L. Teh, A. H. All, O. F. Mohammed, O. M. Bakr, T. Wu, M. Bettinelli, H. Yang, W. Huang and X. Liu, *Nature*, 2018, **561**, 88.
4 J. Zhao, Z. Fan, S. Zhou, Z. Wang, K. Wang, R. Ye, Y. Hua, L. Huang, X. Zhang, L. Lei and S. Xu, *Adv. Funct. Mater.*, 2025, 2305564.
5 S. Guo, K. Liu, Z. Lin, Z. Kang, J. Liu, Z. Yin, Z. Cai, Y. Liu, X. Zhang, F. Luo, S. Xiong, S. Wang, X. He, A. Yue, Q. Zhao, R. Guo and T. Wang, *J. Lumin.*, 2025, **277**, 120956.
6 X. Wang, Y. Dai, Z. Zhang, L. Su, H. Kou, Y. Wang and A. Wu, *J. Rare Earths*, 2021, **39**, 1533–1539.
7 T. Wang, S. Hu, T. Ji, X. Zhu, G. Zeng, L. Huang, A. N. Yakovlev, J. Qiu, X. Xu and X. Yu, *Laser Photonics Rev.*, 2024, **18**, 2300892.
8 S. Wang, J. Yang, C. Liu, W. Li, X. Zheng, X. Qiao, X. Sun, S. Qian, J. Han, J. Wu, X. Xu, J. Ren and J. Zhang, *Laser Photonics Rev.*, 2025, **19**, 2401611.
9 B. Yang, L. Yin, G. Niu, J. H. Yuan, K. H. Xue, Z. Tan, X. S. Miao, M. Niu, X. Du, H. Song, E. Lifshitz and J. Tang, *Adv. Mater.*, 2019, **31**, 1904711.
10 M. Koshimizu, *Jpn. J. Appl. Phys.*, 2022, **62**, 010503.
11 W. Ma, Y. Su, Q. Zhang, C. Deng, L. Pasquali, W. Zhu, Y. Tian, P. Ran, Z. Chen, G. Yang, G. Liang, T. Liu, H. Zhu, P. Huang, H. Zhong, K. Wang, S. Peng, J. Xia, H. Liu, X. Liu and Y. M. Yang, *Nat. Mater.*, 2021, **21**, 210–216.
12 H. Lu, Z. Zheng, H. Hou, Y. Bai, J. Qiu, J. Q. Wang and J. Lin, *Sci. Adv.*, 2023, **11**, 2305378.
13 H. Cui, W. Zhu, Y. Deng, T. Jiang, A. Yu, H. Chen, S. Liu and Q. Zhao, *Aggregate*, 2023, **5**, e454.
14 W. Zhang, W. Zheng, L. Li, P. Huang, J. Xu, W. Zhang, Z. Shao and X. Chen, *Adv. Mater.*, 2024, **36**, 2408777.

15 Y.-P. Lin, S. Hu, J. Xu, Z. Zhang, X. Qi, X. Lu, J. Jin, X.-Y. Huang, Q. Xu, Z. Deng, Z. Xiao and K.-Z. Du, *Chem. Eng. J.*, 2023, **468**, 143818.
16 J.-C. Jin, N.-N. Shen, Z.-P. Wang, Y.-C. Peng and X.-Y. Huang, *Coord. Chem. Rev.*, 2021, **448**, 214185.
17 Y.-P. Lin, X. Lu, Z. Zhang, X. Qi, J. Jin, J. Xu, Y. Wu, Y. Wu, Z. Deng, X.-Y. Huang, C. Han, S. Hu and K.-Z. Du, *Chem. Eng. J.*, 2024, **479**, 147523.
18 Z. Wang, Z. Zhang, L. Tao, N. Shen, B. Hu, L. Gong, J. Li, X. Chen and X. Huang, *Angew. Chem., Int. Ed.*, 2019, **58**, 9974–9978.
19 Z. Zhang, Y. Lin, J. Jin, L. Gong, Y. Peng, Y. Song, N. Shen, Z. Wang, K. Du and X. Huang, *Angew. Chem., Int. Ed.*, 2021, **60**, 23373–23379.
20 J.-C. Jin, Y.-P. Lin, D.-Y. Chen, B.-Y. Lin, T.-H. Zhuang, W. Ma, L.-K. Gong, K.-Z. Du, J. Jiang and X.-Y. Huang, *Inorg. Chem. Front.*, 2021, **8**, 4474–4481.
21 Z. Gong, J. Zhang, X. Deng, M. P. Ren, W. Q. Wang, Y. J. Wang, H. Cao, L. Wang, Y. C. He and X. W. Lei, *Aggregate*, 2024, **5**, e574.
22 V. Morad, Y. Shynkarenko, S. Yakunin, A. Brumberg, R. D. Schaller and M. V. Kovalenko, *J. Am. Chem. Soc.*, 2019, **141**, 9764–9768.
23 Y. Nan, C. Wang, G. Zhang, Z. Kuang, W. Liu, M. Zhou, X. Zhang, S. Dai, P. Ran, X. Xu, Q. Chen, Y. Yang, L. Zhu, Q. Peng, N. Wang and J. Wang, *Adv. Opt. Mater.*, 2024, **12**, 2401158.
24 M. L. Zaffalon, Y. Wu, F. Cova, L. Gironi, X. Li, V. Pinchetti, Y. Liu, M. Imran, A. Cemmi, I. Di Sarcina, L. Manna, H. Zeng and S. Brovelli, *Adv. Funct. Mater.*, 2023, **33**, 2305564.
25 T. B. Shonde, M. Chaaban, H. Liu, O. J. Olasupo, A. Ben-Akacha, F. G. Gonzalez, K. Julevich, X. Lin, J. S. R. V. Winfred, L. M. Stand, M. Zhuravleva and B. Ma, *Adv. Mater.*, 2023, **35**, 1.
26 K. Han, K. Sakhatskyi, J. Jin, Q. Zhang, M. V. Kovalenko and Z. Xia, *Adv. Mater.*, 2022, **34**, 2110420.
27 J. H. Chen, J. B. Luo, Q. P. Peng, Z. L. He, J. H. Wei and D. B. Kuang, *Angew. Chem., Int. Ed.*, 2025, **64**, e202508536.
28 G. Dong, B. Hu, C. Chen, H. Yu, Q. Han and W. Wu, *Inorg. Chem.*, 2024, **63**, 20830–20839.
29 J.-H. Chen, J.-B. Luo, Z.-L. He, Q.-P. Peng, J.-H. Wei, Z.-Z. Zhang, X.-X. Guo and D.-B. Kuang, *Chem. Sci.*, 2025, **16**, 9375–9384.
30 S. Wang, Y. Xu, T. Chen, W. Jiang, J. Liu, X. Zhang, W. Jiang and L. Wang, *Chem. Eng. J.*, 2021, **404**, 125912.
31 Y. Wei, H. Yang, Z. Gao, X. Yun, G. Xing, C. Zhou and G. Li, *Laser Photonics Rev.*, 2020, **15**, 2000048.
32 Y. Wei, H. Yang, Z. Gao, Y. Liu, G. Xing, P. Dang, A. A. A. Kheraif, G. Li, J. Lin and R. S. Liu, *Sci. Adv.*, 2020, **7**, 1903060.
33 P. Dang, W. Wang, H. Lian, G. Li and J. Lin, *Adv. Opt. Mater.*, 2022, **10**, 2102287.
34 X. Zhu, J. Wu, B. Qu, X. Wang, C. Yin and S. Ye, *J. Phys. Chem. C*, 2024, **128**, 1800–1808.
35 S. Ahmad, P. Fu, S. Yu, Q. Yang, X. Liu, X. Wang, X. Wang, X. Guo and C. Li, *Joule*, 2019, **3**, 794–806.
36 W. Li, H. Zhang, C. Yu, T. Li, X. Zhang, C. Xiong and T. Wang, *ACS Appl. Electron. Mater.*, 2021, **3**, 4912–4918.
37 K. Li, Z. Huang, H. Zai, Z. Zhang, F. Wang, X. Zhu, Y. Wu, Y. Zhang, F. Pei, R. Fan, X. Niu, Y. Chen, H. Liu, R. Yin, X. Zhuang, J. A. Steele, C. Zhu, Y. Chen, T. Song, Q. Chen and H. Zhou, *Adv. Mater.*, 2025, **38**, e17685.
38 X. Liu, K. E. O'Harra, J. E. Bara and C. H. Turner, *J. Phys. Chem. B*, 2021, **125**, 3653–3664.
39 X. Du, X. Lu, J. Zhao, Y. Zhang, X. Li, H. Lin, C. Zheng and S. Tao, *Adv. Funct. Mater.*, 2019, **29**, 1902078.
40 C. Wang, Z. Sun, Y. Liu, L. Liu, X. Yin, Q. Hou, J. Fan, J. Yan, R. Yuan, M. Zheng and Q. Dong, *Nat. Commun.*, 2024, **15**, 6292.
41 J.-B. Luo, J.-H. Wei, Z.-L. He, J.-H. Chen, Q.-P. Peng, Z.-Z. Zhang and D.-B. Kuang, *Chem. Sci.*, 2024, **15**, 16338–16346.
42 L.-J. Xu, X. Lin, Q. He, M. Worku and B. Ma, *Nat. Commun.*, 2020, **11**, 4329.
43 L.-K. Gong, Q.-Q. Hu, F.-Q. Huang, Z.-Z. Zhang, N.-N. Shen, B. Hu, Y. Song, Z.-P. Wang, K.-Z. Du and X.-Y. Huang, *Chem. Commun.*, 2019, **55**, 7303–7306.
44 F. Lin, H. Tong, H. Lin and W. Liu, *Chem. Commun.*, 2022, **58**, 12596–12599.
45 J. Lin, Z. Guo, N. Sun, K. Liu, S. He, X. Chen, J. Zhao, Q. Liu and W. Yuan, *Inorg. Chem.*, 2022, **61**, 15266–15272.
46 A. L. Spek, *Acta Crystallogr., Sect. D: Biol. Crystallogr.*, 2009, **65**, 148–155.
47 L. J. Farrugia, *J. Appl. Crystallogr.*, 1999, **32**, 837–838.
48 C. H. Suresh, G. S. Remya and P. K. Anjalikrishna, *Wiley Interdiscip. Rev.: Comput. Mol. Sci.*, 2022, **12**, e1601.
49 M. A. Spackman and D. Jayatilaka, *CrystEngComm*, 2009, **11**, 19–32.
50 M. A. Spackman and J. J. McKinnon, *CrystEngComm*, 2002, **4**, 378–392.
51 L. Mao, P. Guo, S. Wang, A. K. Cheetham and R. Seshadri, *J. Am. Chem. Soc.*, 2020, **142**, 13582–13589.
52 L. Mao, Y. Wu, C. C. Stoumpos, B. Traore, C. Katan, J. Even, M. R. Wasielewski and M. G. Kanatzidis, *J. Am. Chem. Soc.*, 2017, **139**, 11956–11963.
53 H. Deng, K. Huang, L. Xiu, W. Sun, Q. Yao, X. Fang, X. Huang, H. A. A. Noreldeen, H. Peng, J. Xie and W. Chen, *Nat. Commun.*, 2022, **13**, 3381.
54 X.-K. Wan, X.-S. Han, Z.-J. Guan, W.-Q. Shi, J.-J. Li and Q.-M. Wang, *Nat. Commun.*, 2024, **15**, 7214.
55 H. Yu, J. Liu, Q. Hu, J. Liu and W. Wu, *Appl. Surf. Sci.*, 2023, **641**, 158507.
56 C. Li, X. Bai, Y. Guo and B. Zou, *ACS Omega*, 2019, **4**, 8039–8045.
57 H.-Q. Yao, Z. Ding, S.-Y. Zhang, Y.-F. Wu, X. Qiu, Y. Peng, H.-Y. Ye and Z.-B. Hu, *CrystEngComm*, 2024, **26**, 1767–1772.
58 G. Zhou, Z. Liu, M. S. Molokeev, Z. Xiao, Z. Xia and X.-M. Zhang, *J. Mater. Chem. C*, 2021, **9**, 2047–2053.
59 D.-Y. Li, J.-H. Wu, X.-Y. Wang, X.-Y. Zhang, C.-Y. Yue and X.-W. Lei, *Chem. Mater.*, 2023, **35**, 6598–6611.
60 Q. Hu, H. Yu, S. Gong, Q. Han and W. Wu, *J. Mater. Chem. C*, 2022, **10**, 6002–6008.

61 Q. Qiu, G. Zhang, J. Chen, Y. Di, L. Wu, H. Chen, S. C. Chen and M. J. Lin, *Small*, 2024, **21**, 2407346.
62 Y. Zhang, J. Liu, M. Liao, Y. Xu, G. Luo and M. Xia, *Cryst. Growth Des.*, 2025, **25**, 5284–5292.
63 X. Zhao, G. Niu, J. Zhu, B. Yang, J.-H. Yuan, S. Li, W. Gao, Q. Hu, L. Yin, K.-H. Xue, E. Lifshitz, X. Miao and J. Tang, *J. Phys. Chem. Lett.*, 2020, **11**, 1873–1880.
64 Y. Zhang, R. Sun, X. Ou, K. Fu, Q. Chen, Y. Ding, L.-J. Xu, L. Liu, Y. Han, A. V. Malko, X. Liu, H. Yang, O. M. Bakr, H. Liu and O. F. Mohammed, *ACS Nano*, 2019, **13**, 2520–2525.
65 V. V. Nagarkar, T. K. Gupta, S. R. Miller, Y. Klugerman, M. R. Squillante and G. Entine, *IEEE Trans. Nucl. Sci.*, 1998, **45**, 492.
66 J. H. Heo, D. H. Shin, J. K. Park, D. H. Kim, S. J. Lee and S. H. Im, *Adv. Mater.*, 2018, **30**, 1801743.
67 W. Tan, Y. Xiao, C. Zhou, X. Jin, S. Zhu, M. Han, Z. Tang, Y. Zhang, Z. Su, T. Chen, Q. Chen, Q. Liang, W. Chen and Y. Jiang, *Adv. Funct. Mater.*, 2024, **34**, 2406839.
68 (*a*) CCDC 2475506: Experimental Crystal Structure Determination, 2026, DOI: 10.5517/ccdc.csd.cc2p2z1t; (*b*) CCDC 2475507: Experimental Crystal Structure Determination, 2026, DOI: 10.5517/ccdc.csd.cc2p2z2v; (*c*) CCDC 2475508: Experimental Crystal Structure Determination, 2026, DOI: 10.5517/ccdc.csd.cc2p2z3w; (*d*) CCDC 2475509: Experimental Crystal Structure Determination, 2026, DOI: 10.5517/ccdc.csd.cc2p2z4x; (*e*) CCDC 2514806: Experimental Crystal Structure Determination, 2026, DOI: 10.5517/ccdc.csd.cc2qdvss; (*f*) CCDC 2514807: Experimental Crystal Structure Determination, 2026, DOI: 10.5517/ccdc.csd.cc2qdvtt.